photonics

MDPI

Article

Cost-Effective and Drift-Resistant Fiber-Optic Ultrasound Detection with Slope-Symmetric Fabry–Perot Sensor and AOM-Enabled Quadrature Demodulation

Yufei Chu [1,2,*], Xiaoli Wang [2], Mohammed Alshammari [2], Zi Li [3] and Ming Han [2]

[1] School for Environment and Sustainability (SEAS), University of Michigan, Ann Arbor, MI 48109, USA
[2] Department of Electrical and Computer Engineering, Michigan State University, East Lansing, MI 48824, USA
[3] Department of Physics and Engineering, Alma College, Alma, MI 48801, USA
* Correspondence: chuyufei@ustc.edu

Abstract

A robust and cost-effective fiber-optic ultrasound sensor based on a slope-symmetric Fabry–Perot interferometer (FPI) is presented, employing dual-channel quadrature-biased heterodyne interrogation with an acousto-optic modulator (AOM). By introducing a 200 MHz frequency shift that yields an effective $\pi/2$ phase offset between the direct (unshifted) and frequency-shifted optical paths, the system ensures complementary sensitivity: when one channel operates at zero slope on the FPI transfer function (minimum sensitivity), the other resides at maximum slope, providing inherent immunity to laser wavelength drift and environmental perturbations. Experimental validation demonstrates reliable ultrasound detection across varying operating points. At quadrature extremes, one channel achieves peak amplitudes of ± 2 V while the other is quiescent, whereas intermediate points enable simultaneous detection with amplitudes of ± 1.5 V (AOM channel) and ± 0.05–0.1 V (direct channel), accompanied by corresponding DC levels ranging from ~0.4 V to 1.6 V. The AOM channel utilizes simple envelope detection after 9.5–11.5 MHz bandpass filtering, maintaining low cost, though coherent mixing is suggested for enhanced weak-signal performance. The angle-symmetric FPI design, combined with gold-disk reflector adaptations and potential femtosecond laser micromachining, further reduces fabrication costs without sacrificing finesse or sensitivity. This quadrature-biased approach offers superior stability compared to single-channel systems, making it highly suitable for practical applications in photoacoustic imaging, nondestructive testing, and structural health monitoring.

Keywords: Fabry–Perot interferometer; fiber-optic sensor; acousto-optic modulator; quadrature demodulation; ultrasound sensing; slope-symmetric

Received: 21 January 2026
Revised: 16 February 2026
Accepted: 9 March 2026
Published: 11 March 2026

1. Introduction

Fabry–Perot (FP) etalons have found widespread application in various fields, such as optical fiber sensing and lidar detection, due to their exceptional spectral characteristics [1–5]. Fiber-optic sensors have revolutionized sensing technologies due to their inherent advantages, including immunity to electromagnetic interference, compact size, lightweight construction, and capability for remote and distributed measurements [6–8]. These sensors operate by modulating light properties such as intensity, phase, wavelength, or polarization in response to external stimuli, making them ideal for harsh environments like high-voltage systems or biomedical settings [7,8]. Building on this foundation, fiber-optic Fabry–Perot interferometers (FPIs) have emerged as a specialized subset, offering exceptional sensitivity for detecting

a wide range of physical parameters [7,9]. In temperature sensing, the demand for high-precision environmental monitoring within Cyber-Physical-Social Systems by successfully developing and empirically validating a novel high-sensitivity temperature sensor was reported [10]. For vibration and strain monitoring, they convert mechanical displacements into phase shifts, enabling real-time structural health assessment in bridges or aircraft [8]. Particularly noteworthy is their role in acoustic and ultrasonic detection, where FPIs transduce sound waves or ultrasound-induced pressure variations into optical signals, providing high-frequency responses up to several MHz with minimal cross-sensitivity to other measurands [9,11]. This versatility stems from the FPI's low-finesse or high-finesse configurations, which can be tailored for specific applications, such as in vivo medical diagnostics or industrial noise monitoring [7,8].

Current research on fiber-optic FP ultrasonic sensors has advanced significantly, focusing on enhancing sensitivity, bandwidth, and integration for practical applications [9–16]. Studies have demonstrated their efficacy in partial discharge detection within power transformers, where ultrasonic emissions from insulation breakdowns are captured with high spatial resolution, aiding in preventive maintenance and reducing outage risks [15]. In medical diagnostics, FP sensors enable non-invasive ultrasonic imaging, such as photoacoustic tomography [13,14]. Recent developments include an ultrasonic sensor system based on a low-finesse FPI formed by two weak chirped fiber Bragg gratings (CFBGs) on a coiled single-mode fiber [11,12]. Furthermore, hybrid configurations combining FPIs with Bragg gratings have been explored for omnidirectional sensing, expanding their use in structural health monitoring of composites or pipelines [16]. Ongoing efforts emphasize multiplexing multiple FP sensors in arrays for distributed ultrasonic mapping, with field trials showing robust performance in noisy environments [13].

Despite these advancements, existing fiber-optic FP ultrasonic sensing technologies face substantial challenges that hinder widespread adoption [4,5,17–19]. Numerous demodulation schemes, such as phase-generated carrier (PGC) methods, have been developed to extract ultrasonic signals with high fidelity, yet they often significantly escalate sensor production costs [4,19]. Additionally, interrogation systems demand expensive, wavelength-stable laser sources to maintain the quadrature operating point, as environmental perturbations like temperature fluctuations can cause fringe fading, degrading the signal-to-noise ratio (SNR) [18,19]. These issues not only increase overall system expenses but also compromise reliability in dynamic field conditions, limiting scalability for industrial applications such as power grid monitoring or large-scale biomedical imaging [4,17].

Although acousto-optic modulator (AOM)-based frequency-shift interrogation techniques have been successfully implemented in experiments, sensor costs remain high in prior designs due to the need for precise matching of two fiber Bragg gratings' reflectance spectra. Building upon the methodology established in our prior work [20], this study proposes a robust and cost-effective interrogation system that integrates a low-cost, angle-tunable FP sensor with an AOM-based dual-path demodulation scheme [12]. The AOM approach provides reliable quadrature demodulation (with an effective 90° phase difference) that mitigates environmental drift in the FP sensor response, ensuring at least one detection channel operates on a high-sensitivity slope. The key innovations of the present work are threefold: (1) the adoption of an angle-tunable gold-disk FP sensor, which simultaneously extends the operational spectral coverage of the Fabry–Pérot cavity and significantly reduces fabrication cost through simple tilt-angle optimization of rear reflectance; (2) the implementation of a AOM-based frequency shift to enable simultaneous acquisition of both a direct baseband signal and a modulated heterodyne carrier signal, deliberately introducing a quadrature phase bias between the two paths; the resulting inherent robustness against wavelength-induced operating point variations—ensuring that at least one

detection channel always operates near the maximum sensitivity point without requiring active wavelength stabilization or expensive frequency-locking hardware. The paper is organized as follows: Sections 2.1 and 2.2 describes the sensor fabrication and angle-tuning mechanism; Sections 2.3–2.5 presents the theoretical framework of AOM-enabled quadrature demodulation; Section 3 details the experimental setup and measurement results; and Section 4 provides conclusions together with discussions on future research directions and potential optimizations.

2. Methodology and Principle

2.1. Manufacturing Process and Reflectance Matching

The sensor is fabricated through a streamlined process that ensures high-reflectivity matching and spectral symmetry [12]. First, the front FPI cavity is created on the fiber tip using excimer laser (XCL) UV etching, with laser power and exposure time precisely controlled to achieve the desired reflectivity R1 [21]. The fiber end-face is then positioned on a 3D translation stage, and a 600 μm gold disk reflector is carefully aligned under electron microscopy for gentle contact with the fiber tip. Next, a small amount of UV glue (0.5 mL) is applied between the disk and the fiber, and stress is gently applied to adjust the disk's tilt angle while monitoring the transmittance curve in real time until symmetrical slopes are obtained, resulting in a nearly sinusoidal reflectance response. Once the optimal angle is reached, it is permanently fixed by UV curing. The use of a gold disk reflector provides nearly wavelength-independent reflectance over a broad range, allowing the spectral characteristics of the front FPI to dominate and greatly simplifying laser wavelength tuning to the point of maximum slope for optimal linearity and sensitivity.

The crux of the fabrication process lies in the precise matching of the rear reflectance with the front-end reflectance. As illustrated in Figure 1, a precision fiber fixture is employed to maintain contact between the fiber end-face and a high-reflectivity gold disk. The optical signal from a Tunable Semiconductor Laser (TSL) passes through a phase controller and an optical circulator before entering a Chirped Fiber Phase Grating (CFPG). After propagating through a fiber length of approximately 39 cm [6], the light emerges from the fiber tip and impinges upon the gold disk. While a portion of the light dissipates into free space, a significant fraction is reflected back into the fiber core. This optical feedback establishes a resonance between the CFPG and the gold disk, thereby forming a long-cavity Fabry–Perot (FP) interferometer. The interference signal propagates backward through the circulator and is captured by a Photodetector (PD), allowing for real-time monitoring of the reflectance spectrum via an oscilloscope or an Optical Spectrum Analyzer (OSA).

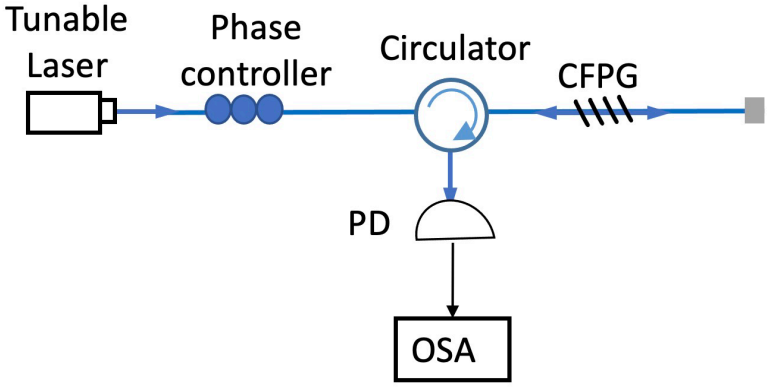

Figure 1. The FP rear reflectivity detection device.

Unlike conventional approaches that rely on precisely controlling a fixed tilt angle to achieve a target reflectance, our method prioritizes direct matching of the effective

reflectance rather than a specific angular value. This is necessary because the CFPG reflectivity varies slightly from device to device due to fabrication tolerances, precluding the use of a universal fixed-angle setting. The tuning is achieved using a simple, practical mechanical approach on a standard three-dimensional optical breadboard platform. The output fiber (with the CFPG at its cleaved end-face) is securely held in a Thorlabs T711 post-mountable fiber clamp (a precision V-groove clamp designed for buffered fibers, mounted via M4 tap to a post or rail carrier). The fiber clamp is positioned vertically, and the gold disk is placed flat on the horizontal breadboard surface. The fiber end-face is initially aligned coaxially above the gold disk at a nominal separation of ~100–200 μm (adjusted for optimal fringe visibility during monitoring). Fine tuning is performed by controllably varying the vertical position of the fiber clamp mount (via micrometer-driven translation stages on the 3D platform). This applies adjustable mechanical stress to the fiber buffer against the rigid gold disk, inducing a small, controllable tilt of the fiber end-face relative to the mirror plane. The resulting change in the effective cavity coupling and fringe visibility is monitored in real time using the wavelength-swept reflectance measurement (as shown in Figure 2). The tilt-induced adjustment allows precise matching of the FP cavity's peak-to-peak reflectance amplitude and slope symmetry to the specific reflectivity characteristics of the individual CFPG, ensuring optimal linear operating range for ultrasound detection.

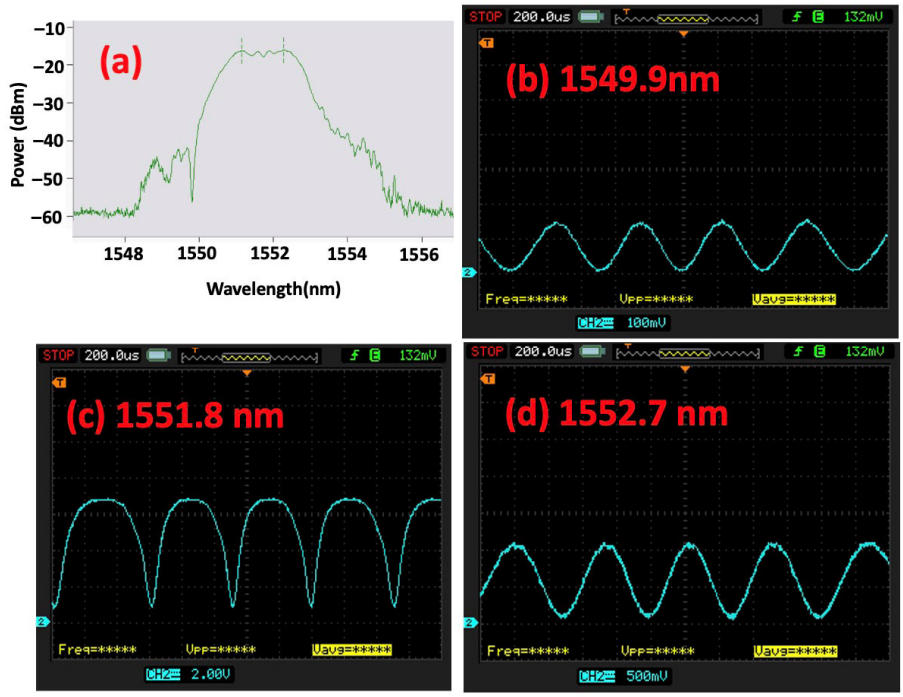

Figure 2. Reflectance spectra of the fiber-optic FPI as a function of wavelength: (**a**) Measured reflectance of the front-end Chirped Fiber Phase Grating (CFPG); (**b**–**d**) Time-domain interferometric reflectance curves of the FP cavity (formed by the CFPG and rear gold disk) recorded during wavelength scanning at center wavelengths of 1549.9 nm, 1551.8 nm, and 1552.7 nm, respectively. *X*-axis: Time (200.0 μs/div), corresponding to the laser wavelength sweep. *Y*-axis: Reflected intensity on CH2 (100 mV/div in (**b**), 2.00 V/div in (**c**), 500 mV/div in (**d**)). These traces illustrate the wavelength-dependent fringe visibility and slope of the FP sensor response.

Once the desired reflectance profile is achieved, approximately 0.5 mL of UV-curable adhesive is dispensed at the fiber-disk junction to permanently fix the geometry. Upon UV curing, a minor shift in the effective optical path length and reflectance occurs due to the refractive index change introduced by the glue. After curing, the tilt mechanism is locked, and the sensor loses its active tunability. Subsequently, the ~39 cm length

of fiber between the CFPG and the gold disk is coiled into a compact disk (~5–7 cm diameter) for practical packaging and deployment. This coiling step introduces negligible additional perturbation but allows minor compensation for any residual post-cure drift through slight mechanical relaxation or environmental stabilization [4,12]. At this stage, the sensor's operating wavelength window and slope are fixed and no longer require further rear-mirror adjustment [12,17]. Thus, the "angle-tunable" aspect refers specifically to the pre-curing fabrication stage, where the design enables flexible, device-specific optimization of reflectance matching in the lab—achieving performance comparable to (or better than) dual-FBG configurations but at a fraction of the cost and complexity.

2.2. Spectral Optimization and Wavelength Extension

To broaden the operational bandwidth of the sensor, various front-end CFPGs are fabricated using different chirped masks. Figure 2a displays a representative reflectance spectrum with a full-width at half-maximum (FWHM) spanning from 1551 nm to 1553 nm. By selecting specific interrogation wavelengths and adjusting the tilt angle of the rear gold disk, the interference fringe profile can be precisely tailored.

For instance, at wavelengths of 1549.9 nm (Figure 2b) and 1552.7 nm (Figure 2d), the interference curves exhibit a quasi-sinusoidal profile with highly symmetrical slopes, which is optimal for linear demodulation. Conversely, at 1551.8 nm (Figure 2c), the spectrum becomes distorted and asymmetrical, making it unsuitable for high-precision sensing. It is noteworthy that since the reflectivity of the gold disk is nearly wavelength-independent, we can strategically select the working wavelength based on specific application scenarios. Configurations such as those shown in Figure 2b,d are highly resilient to laser frequency drift or environmental fluctuations, whereas the configuration in Figure 2c could be utilized in stable environments where a stronger echo signal is required.

After the optimal wavelength and alignment angle are finalized, the assembly is permanently stabilized through UV curing. To further enhance the sensor's sensitivity to ultrasonic vibrations, the fiber section within the FP cavity is coiled into a disk configuration with an inner diameter of ~6 mm and an outer diameter of ~8 mm, following the optimization strategies described in our previous works [4,11,12,17].

2.3. Based Dual-Path Interrogation Principle

While the coiled FPI sensor described above is capable of detecting ultrasound signals using the setup in Figure 1, its performance is highly sensitive to environmental perturbations such as temperature-induced wavelength drift. Such drift shifts the laser wavelength away from the optimal quadrature point, leading to significant signal fading or distortion. Conventional solutions to this problem, such as active laser frequency locking or high-speed electro-optic modulator (EOM)-based PGC schemes [4,17], provide high stability but are often cost-prohibitive for large-scale industrial deployment.

In this work, we propose a cost-effective alternative utilizing an AOM in a dual-path configuration. As illustrated in Figure 3, the laser output is split into two paths—I_{10} and I_{20}—via a 1 × 2 beam splitter. The first path (I_{10}) is directly connected to one input of a 2 × 1 fiber coupler. The second path (I_{20}) passes through an AOM for frequency modulation before entering the other input of the coupler. The intensity of this modulated path can be represented as:

$$I_{20}(1 + kcos\gamma t), \tag{1}$$

where k is the modulation depth and γ is the carrier frequency. The combined light from the 2 × 1 coupler is directed to the sensor via an optical circulator. The FPI sensor, which incorporates a coiled fiber structure (inner diameter ~6 mm, outer diameter ~8 mm) for

enhanced sensitivity [4,12], reflects the light back through the circulator to a PD. Assuming the reflectance of the FP sensor is:

$$R = A + B\cos(\theta_0 + \Delta\theta), \tag{2}$$

where $\theta = \theta_0 + \Delta\theta$ and θ_0 is the static phase and $\Delta\theta$ is the ultrasound-induced phase shift, Here, A represents the average (DC) reflectance, which arises from the baseline reflectivity and any mismatch between the two cavity mirrors, while B denotes the amplitude of the interference modulation (AC component), which depends on the reflectivity matching, cavity finesse, and losses. The total signal $g(t)$ captured by the PD is given by:

$$g(t) = I_{10}(A + Bcos\theta) + I_{20}(1 + kcos\gamma t)[A + Bcos(\theta + \alpha)], \tag{3}$$

where α represents the phase difference introduced by the optical path length mismatch between the two arms.

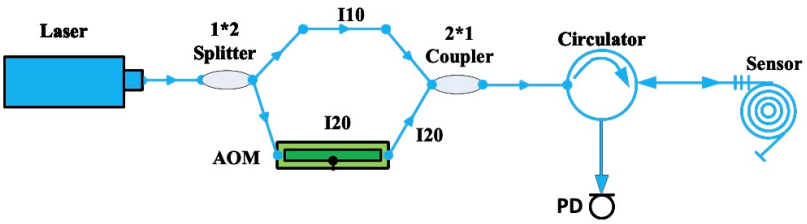

Figure 3. Schematic diagram of the proposed AOM-based dual-path demodulation scheme.

The dual-path architecture requires careful design to introduce a quadrature phase difference (90°) between the two arms, thereby deliberately creating complementary signal characteristics: one path delivers the direct baseband signal, while the other provides a carrier-modulated signal. Thanks to this engineered 90° phase offset, when laser wavelength drift causes the operating point of one path to shift to a peak or valley of the interference fringe—where sensitivity to the ultrasound signal is lost—the other path (or its modulated carrier component) remains capable of effectively detecting the high-frequency ultrasound signal. This built-in redundancy mechanism significantly enhances system robustness, enabling reliable, continuous monitoring without the need for costly frequency-locking hardware.

2.4. Mathematical Derivation and Signal Decomposition

To analyze the response of the dual-path interrogation system to ultrasonic waves, we consider the phase perturbation $\Delta\theta(t)$ induced by the acoustic signal. Under the condition where the ultrasonic-induced phase shift is significantly smaller than the carrier modulation depth ($\Delta\theta \ll 1$), we can apply the small-signal approximation using the first-order Taylor expansion:

$$\cos(\theta_0 + \Delta\theta) \approx \cos\theta_0 - \Delta\theta sin\theta_0, \tag{4}$$

$$\cos(\theta_0 + \Delta\theta + \alpha) \approx \cos(\theta_0 + \alpha) - \Delta\theta sin(\theta_0 + \alpha). \tag{5}$$

Substituting these approximations into the general expression for the detected signal $g(t)$, we obtain:

$$g(t) = I_{10}[\mathrm{A} + \mathrm{B}(\cos\theta_0 - \Delta\theta sin\theta_0)] + I_{20}(1 + kcos\gamma t)[A + B(\cos(\theta_0 + \alpha) - \Delta\theta sin(\theta_0 + \alpha))]. \tag{6}$$

By expanding the brackets and grouping the terms according to their physical characteristics (DC components, baseband signal components, and modulated carrier components), the expression for $g(t)$ can be reorganized as follows:

$$g(t) = g_{DC} + g_{Baseband} + g_{Carrier.} \tag{7}$$

(1) DC and Static Component (g_{DC}):

This term represents the constant background intensity and the static interference state determined by the initial cavity phase θ_0.

$$g_{DC} = I_{10}(\mathrm{A} + \mathrm{B}\cos\theta_0]) + I_{20}(A + B\cos(\theta_0 + \alpha)). \tag{8}$$

(2) Direct Baseband Signal Component ($g_{Baseband}$):

This term represents the low-frequency ultrasound signal captured directly by the two paths. It is the superposition of the signals from the I_{10} and I_{20} paths. The baseband component contains the vibration information captured directly by the FPI sensor:

$$g_{Baseband} = -[I_{10}B\sin\theta_0 + I_{20}\,\mathrm{B}\sin(\theta_0 + \alpha)]\Delta\theta(t). \tag{9}$$

In practical implementation, this signal path is processed using a Bandpass Filter (BPF, Thorlabs, Ann Arbor, MI, USA) with a passband of 50 kHz to 1 MHz. This specific filtering range serves a dual purpose: it effectively suppresses 1/f noise and low-frequency phase fluctuations caused by ambient temperature changes or slow mechanical drifts (typically <10 kHz), while simultaneously preserving the high-frequency components of the ultrasonic wave. This path provides a direct, low-latency observation of the acoustic event when the sensor is operating near its quadrature point.

(3) AOM Modulated Carrier Component ($g_{Carrier}$):

This term consists of the high-frequency carrier introduced by the AOM and its sidebands which contain the ultrasound information.

$$g_{Carrier} = I_{20}k[A + B\cos(\theta_0 + \alpha)]\cos\gamma t - [I_{20}kB\sin(\theta_0 + \alpha)\cos\gamma t]\Delta\theta(t). \tag{10}$$

The first term in Equation (10) exhibits a nearly constant amplitude and carries no ultrasound information (independent of $\Delta\theta(t)$), functioning solely as a strong reference high-frequency carrier sinusoid. Even with drifts in the operating point θ_0, amplitude variations remain limited, as A is typically much larger than $|\,\mathrm{B}\cos(\theta_0 + \alpha)\,|$. The second term corresponds to the carrier sidebands, with frequencies distributed around γ (down-converted to approximately 10 MHz ± ultrasound frequencies). Overall, g_Carrier forms an amplitude-modulated (AM) 10 MHz carrier, where the ultrasound signal is encoded in the modulation envelope.

The carrier component represents the signal up-converted to the AOM modulation frequency (γ). Assuming an AOM modulation frequency of f_{AOM} = 10.5 MHz, the signal is centered at this high-frequency carrier. We employ a high-Q Bandpass Filter (range: 10 MHz to 11 MHz) to isolate this component. Following the filtration, a Low-Cost Envelope Detector (ED) is used to extract the amplitude variations. This path is particularly robust because the high-frequency carrier modulation allows the signal to bypass the high-noise low-frequency regime. Even if the baseband path suffers from significant DC drift, the carrier-to-noise ratio in the MHz range remains high, ensuring reliable detection.

The decomposed equation highlights the core strength of the dual-path architecture:

AOM Carrier Advantage: The final term in the $g_{Carrier}$ expression, $I_{20}k[A + B\cos(\theta_0 + \alpha)]\cos\gamma t$, indicates that the ultrasound signal is up-converted to the

carrier frequency γ. This allows for frequency-domain separation of the signal from low-frequency environmental noise (e.g., vibration and temperature drift), further improving the signal-to-noise ratio (SNR).

Cost-Efficiency: Unlike active wavelength-locking systems that require complex feedback electronics and high-end tunable lasers, this open-loop dual-path configuration provides a passive, robust method to maintain continuous detection stability at a fraction of the cost.

2.5. Sensitivity Redundancy and Offset Optimization

Following the fabrication protocols detailed in Sections 2.1 and 2.2, the FPI sensor was constructed with an effective cavity length of approximately 39 cm. Given the refractive index of the silica fiber medium (n = 1.445), the resulting interference spectrum exhibits an exceptionally high finesse, characterized by a free-spectral range (FSR) of only ~2 pm. While this ultra-narrow linewidth inherently yields superior static sensitivity and high Q-factors, it simultaneously imposes a stringent limitation: the system becomes hypersensitive to laser frequency drifts and environmental thermal fluctuations. A minor wavelength shift can easily move the operating point (Q-point) out of the linear region, leading to signal fading.

The most critical innovation of this dual-path system is the Sensitivity Redundancy provided by the phase offset α. The sensitivity of the baseband and carrier paths are proportional to $\sin\theta_0$ and $\sin(\theta_0 + \alpha)$, respectively. To eliminate the "blind zones" (where $\sin\theta_0 \approx 0$) associated with standard FPI sensors, we strategically set the phase offset $\alpha = \pi/2$.

To mitigate this instability without resorting to complex active feedback loops, we introduced the active phase-shifting mechanism utilizing an AOM. The core principle relies on the non-reciprocal phase accumulation between the direct baseband path and the frequency-shifted carrier path. According to interferometric theory, the phase delay $\Delta\phi$ induced by a frequency shift Δf over a path length L is governed by:

$$\Delta\phi = \frac{2\pi n L \Delta f}{c} \tag{11}$$

In our experimental configuration, with L = 39 cm and an AOM modulation frequency of Δf = 200 MHz, the calculated phase offset is approximately 1.5π. In the context of the interference fringe domain, a 2π phase shift corresponds to one full FSR; therefore, a shift of 1.5π is equivalent to a displacement of 0.75 wavelengths (λ).

This specific phase offset is critical for establishing sensitivity redundancy. By designing the system such that the two interrogation paths are separated by a substantial fraction of the fringe period (0.75 λ), we effectively eliminate "blind spots." When external perturbations—such as ambient temperature variations or laser source instability—cause the operating point of one path to drift toward a peak or valley (where the slope sensitivity approaches zero), the complementary AOM-modulated path is mathematically guaranteed to remain within a high-slope, quasi-linear region. Consequently, this dual-path complementary architecture significantly enhances the sensor's robustness. It ensures reliable capture of transient ultrasound signals even in harsh industrial environments, offering a cost-effective alternative to expensive wavelength-locking hardware. Detailed theoretical derivation and experimental validation of this phase compensation strategy are provided in References [4,12,17].

3. Experimental Setup and Results

3.1. Setup

As shown in the schematic (Figure 4), the experimental setup is a fiber-optic ultrasound detection system based on an FP sensor. The laser wavelength is precisely tuned to 1549.6 nm to match the peak sensitivity or interrogation wavelength of the FP sensor. The continuous-wave laser beam is split by a 1 × 2 fiber splitter with a 1:9 coupling ratio. The lower-power branch (10% of the total intensity, labeled I_{10}) is routed directly to one input port of a 2 × 1 fiber coupler (50:50 splitting ratio). The higher-power branch (90% intensity, labeled I_{20}) passes first through a polarization controller (PC) to optimize the polarization state for maximum diffraction efficiency in the subsequent AOM, then through the AOM itself, and finally to the second input port of the 2 × 1 coupler.

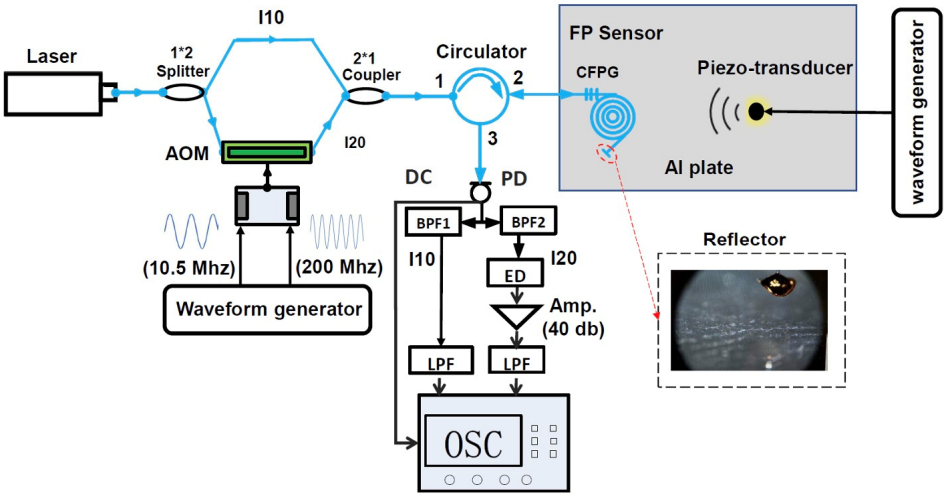

Figure 4. Schematic of the ultrasound detection setup integrating an angle-symmetric Fabry–Perot (FP) sensor and an acousto-optic modulator (AOM). Key components and parameters: laser wavelength, 1549.6 nm; 1 × 2 fiber splitter (9:1 splitting ratio); 2 × 1 fiber coupler (50:50); bandpass filter BPF1 (50 kHz–1 MHz); bandpass filter BPF2 (9.5 MHz–11.5 MHz); low-pass filter (LPF, cutoff frequency < 500 kHz).

To AOM, also known as a Bragg cell, operates based on the acousto-optic effect. A piezoelectric transducer, driven by a radio-frequency (RF) signal, generates a traveling acoustic wave (typically at ~100–400 MHz) within a transparent crystal (e.g., TeO_2 or quartz). This acoustic wave induces a periodic modulation of the refractive index via the photoelastic effect, forming a moving diffraction grating. When the incident laser beam satisfies the Bragg condition (incident angle tuned to achieve high diffraction efficiency into the first order), the light is efficiently diffracted into the +1st order (or −1st order, depending on geometry), while the 0th order (undiffracted beam) is suppressed or used separately. In the Bragg regime—which is the standard operating mode for most fiber-coupled or free-space AOMs in precision optical systems—the dominant diffracted beam (+1st order in our configuration) experiences a precise optical frequency up-shift equal to the acoustic frequency (here, +200 MHz), due to the Doppler-like interaction with the moving acoustic grating. Simultaneously, the intensity (amplitude) of the diffracted beam can be controlled by varying the RF drive power applied to the transducer [20].

In our setup, the AOM is driven by a composite RF signal that provides both: a fixed carrier at 200 MHz, which imparts the +200 MHz optical frequency shift to the first-order diffracted beam, and an additional amplitude modulation at 10.5 MHz (with drive voltage modulated between 0.6–1.2 V), which imposes a corresponding intensity modulation on the output beam at 10.5 MHz. This dual modulation enables both the frequency tagging

(for heterodyne detection or coherent measurement) and the intensity encoding required for subsequent lock-in demodulation of the ultrasound-modulated optical signal. The output light from the AOM (taken from the first diffraction order) therefore carries both a +200 MHz frequency shift and a 10.5 MHz intensity modulation (Figure 4). This frequency-shifted reference beam (I_{10}) enables heterodyne detection when it interferes with the probe beam returning from the sensor. The combined output of the 2 × 1 coupler is directed to port 1 of an optical circulator. The light exits port 2, travels to the Fabry–Perot ultrasound sensor head attached to an aluminum plate, and the reflected probe beam—now modulated by ultrasound-induced cavity length changes—returns to port 2 and is routed to port 3 of the circulator, then to the photodetector (NEWPORT 1811-FC, NEWPORT, Irvine, CA, USA). Prior to connecting the AOM to the 2 × 1 fiber coupler, the amplitude modulation input and optical frequency shift applied to the AOM were verified to ensure optimal operating conditions. Ultimately, a 10.5 MHz amplitude modulation input of 0.6–1.2 V and an ultrasonic modulation frequency of 200 MHz were selected.

For calibration and testing purposes, a piezoelectric transducer (PZT) mounted on the aluminum plate is driven by a dedicated waveform generator. The generator produces a 150 kHz sinusoidal burst signal consisting of five cycles, with a peak-to-peak amplitude of 5 V and a repetition rate of 40 Hz. Through the converse piezoelectric effect, the applied electrical burst excites mechanical vibrations in the PZT, generating well-controlled ultrasonic waves—typically short acoustic pulses centered at 150 kHz—that propagate through the aluminum plate primarily as guided plate waves (e.g., symmetric or antisymmetric Lamb modes) or bulk longitudinal waves, depending on the plate thickness and excitation conditions.

The FP ultrasound sensor, securely attached to the plate, converts incident ultrasonic waves into optical intensity modulation via multi-beam interference. The interrogation laser is tuned to 1549.6 nm. When ultrasonic pressure induces dynamic strain and minute periodic variations in the cavity length ($\Delta L \ll \lambda$), the interference spectrum shifts accordingly. Operating at a fixed wavelength on the linear slope, these length modulations are linearly transduced into proportional intensity changes in the reflected light, yielding a high-fidelity time-domain representation of the incident ultrasound waveform.

The PD receives this intensity-modulated optical signal and provides both DC and AC electrical outputs. The DC output, which is proportional to the time-averaged optical power, serves as a monitor of overall system stability, laser power fluctuations, and sensor baseline reflectivity; it is recorded directly on channel 2 (CH2) of the oscilloscope (OSC, RIGOL DS1104B, Suzhou, China) or data acquisition card (DAQ, Texas Instruments, Santa Clarita, CA, USA). The AC output contains the dynamic ultrasound-induced modulation and is further processed through parallel signal conditioning paths for detailed analysis.

The AC output is split into two parallel processing paths: Direct low-frequency path: The signal passes through bandpass filter BPF1 (150 kHz–1 MHz) to isolate the primary ultrasound frequency band, followed by a low-pass filter (LPF, cutoff < 500 kHz) to remove high-frequency noise. The filtered signal is recorded on channel 3 (CH3, labeled "DIRECT") of the oscilloscope. This channel captures the baseband ultrasound signal without demodulation. Heterodyne (AOM) path: The signal passes through bandpass filter BPF2 (9.5–11.5 MHz) centered on the 10.5 MHz beat frequency created by the AOM-shifted reference. The filtered carrier is then envelope-detected (ED) to extract the ultrasound modulation, amplified by a 40 dB gain stage, and finally low-pass filtered (LPF, cutoff < 500 kHz) to remove residual carrier components. The resulting demodulated ultrasound signal is recorded on channel 1 (CH1, labeled "AOM") of the oscilloscope.

This dual-path detection scheme allows simultaneous acquisition of the direct interferometric signal and the demodulated heterodyne signal, providing complementary

information about sensor response, phase sensitivity, and signal-to-noise ratio in different frequency regimes. The setup is typical of high-sensitivity fiber-optic ultrasound detection systems used in photoacoustic imaging or non-destructive testing applications.

Even with these considerations, the overall system remains cost-effective relative to previous comparable devices [20,22], especially for multi-sensor or array-based probing. The present setup is based on a prior design from our group [20] but eliminates an intensity modulation stage in Channel 1, reducing electronic complexity. More importantly, the key cost reduction arises from the angle-tunable sensor design: unlike earlier approaches requiring two precisely matched FBGs—where achieving symmetric reflectance slopes via expensive XCL laser-based trimming processes demands high-end equipment and increases fabrication costs—the current sensor uses a single front-end FBG paired with a simple gold disk reflector. By angle-tuning the incident light to optimize the effective reflectance and achieve symmetric slope response, this configuration reduces the sensor head cost to well below one-tenth of the dual-FBG approach while maintaining comparable or improved performance. These savings become particularly significant when deploying multiple sensors, as in potential array applications [22]. Although high-cost items such as the narrow-linewidth laser and AOM are still required for coherent detection, the overall architecture offers meaningful economies in fabrication, alignment, and scalability compared to prior fiber-optic ultrasound interferometric systems.

3.2. Results

As described in Section 2.5, the system is configured to introduce a 90° ($\pi/2$) phase difference between the direct (unshifted) reference arm (I_{10}) and the frequency-shifted arm passing through the acousto-optic modulator (AOM, I_{20}). This quadrature biasing scheme ensures that when the operating point of one arm lies at a slope of zero on the Fabry–Perot (FP) transfer function (i.e., minimum sensitivity), the operating point of the other arm is positioned at the point of maximum slope (i.e., peak sensitivity). This complementary behavior provides robust ultrasound detection across a range of laser wavelength drifts.

Figure 5a,b illustrate this principle experimentally. In Figure 5a, the direct channel (DIRECT) captures a clear ultrasound signal, while the AOM channel shows essentially zero response. Conversely, in Figure 5b, the AOM channel detects a strong ultrasound signal, but the direct channel yields no detectable modulation. These results preliminarily demonstrate that the sensor, when interrogated with the setup shown in Figure 4, reliably operates in at least one detection channel under varying conditions.

To further elucidate the sensor's operating mechanism, consider Figure 5e. The upper subplot shows the FP sensor's reflectivity transfer function (reflectance versus wavelength or effective cavity length), while the lower subplot displays both the reflectance curve and its derivative (slope, which governs interferometric sensitivity to cavity perturbations). Four representative laser interrogation wavelengths are selected for the direct arm (labeled points 1–4), with corresponding operating points after AOM frequency shifting denoted as 1′–4′.

As discussed in Section 2.5, the 200 MHz frequency shift introduced by the AOM corresponds to an optical phase shift of approximately 1.5π (or 0.75 fringe) for the sensor's ~2 pm free spectral range (FSR). Since the transfer function is periodic with 2π, this is equivalent to a net shift of -0.5π (π phase difference, or quadrature). This explains the relative positioning in Figure 5e: for example, point 1′ is displaced leftward from point 1 by 0.25 fringe (0.5π), placing the arms in quadrature.

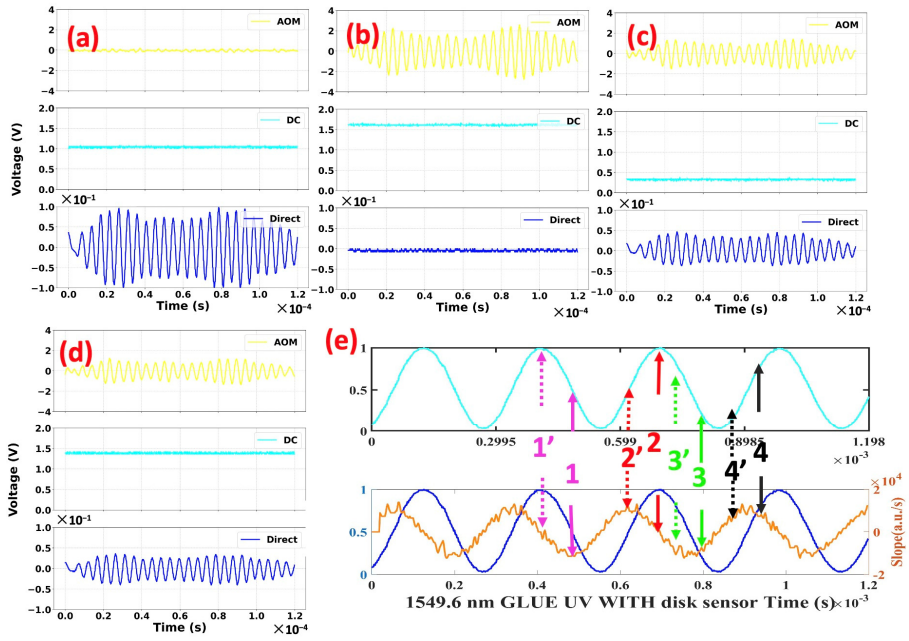

Figure 5. Ultrasound detection results obtained with the angle-symmetric Fabry–Perot (FP) sensor interrogated via an acousto-optic modulator (AOM)-based dual-channel scheme. Panels (**a**–**d**) correspond to operating points 1–4 shown in panel (**e**), respectively. In panel (**e**), the solid lines labeled 1–4 represent the operating points for the direct (baseband) channel, while the dashed lines labeled 1′–4′ denote the corresponding operating points for the AOM (heterodyne) channel; different colors represent different working pairs.

Analysis of operating point 1 (corresponding to Figure 5a): The direct arm wavelength is centered at the midpoint of a reflectance fringe (peak), where the slope is near the negative number with the largest absolute value—yielding max sensitivity to ultrasound-induced cavity modulations. Consequently, the direct channel detects the ultrasound signal that is the most sensitive via baseband intensity modulation. In contrast, the AOM-shifted arm operates near a reflectance peak (maximum reflectivity, slope ≈ 0), resulting in negligible ultrasound response on the heterodyne (AOM) channel. Experimental observations confirm this: the AOM channel amplitude is nearly zero, the DC level (proportional to average power) remains stable at ~1 V (dominated by the high-reflectivity direct arm with 90% power), and the direct channel exhibits modest ultrasound peaks of ±0.1 V.

Analysis of operating point 2 (corresponding to Figure 5b): Here, the direct arm is tuned to a reflectance peak (slope = 0), rendering the direct channel insensitive to ultrasound. The AOM-shifted arm, however, falls near the midpoint of the fringe (steepest slope region), maximizing heterodyne sensitivity. This yields strong ultrasound detection on the AOM channel with amplitudes of ±2 V. The DC level is elevated (~1.6 V) due to high reflectivity at the direct arm's operating point, while the direct channel shows no modulation (~0 V).

Analysis of operating point 3 (corresponding to Figure 5c): The direct arm operates on the left side of a reflectance minimum (valley), where the slope is negative and moderately large (though not maximal). This enables detectable—but not optimal—ultrasound response on the direct channel (±0.05 V amplitude). The AOM-shifted arm is positioned on the right side of a reflectance maximum, with a similarly negative, moderate slope, yielding good but sub-maximal sensitivity on the AOM channel (±1.5 V). Both channels are active. The DC level (~0.4 V) is lower, primarily determined by the direct arm's proximity to a reflectance valley (despite its 90% power weighting), while the AOM arm contributes minimally to the average power.

Analysis of operating point 4 (corresponding to Figure 5d): Symmetrically, the direct arm is on the left side of a reflectance peak (positive, moderate slope), allowing ultrasound

detection on the direct channel (±0.05 V) with reduced sensitivity. The AOM-shifted arm lies on the right side of a reflectance minimum (positive, moderate slope), producing comparable performance on the AOM channel (±1.5 V). Again, both channels detect the signal. The DC level is higher (~1.4 V), reflecting the direct arm's higher reflectivity near the peak.

In summary, the quadrature-biased heterodyne interrogation scheme implemented in the Figure 4 setup, combined with the high-performance yet cost-effective FP sensor, ensures reliable ultrasound detection regardless of laser wavelength drift. At least one channel (direct or AOM) always operates near peak sensitivity, providing inherent robustness against environmental perturbations and long-term stability—key advantages for practical deployment in applications such as photoacoustic imaging or nondestructive testing.

4. Conclusions and Discussion

Building upon the previously developed angle-symmetric fiber-optic FP sensor, this study advances the interrogation methodology by integrating an AOM to enable dual-channel quadrature detection, where the two optical paths (direct and frequency-shifted) maintain a 90° ($\pi/2$) phase offset. This configuration enhances robustness against wavelength drifts and environmental perturbations. The investigation systematically covers the detection principles, including the 200 MHz AOM frequency shift that induces an effective optical phase displacement of approximately 1.5π (equivalent to 0.75 fringes for the sensor's ~2 pm free spectral range, FSR), resulting in a net quadrature bias of 0.5π after periodicity considerations. Subsequent signal processing employs ED for heterodyne demodulation, followed by detailed experimental validation and analysis of various operating points across the FP transfer function.

Experimental results, as illustrated in Figure 5a–d, quantitatively demonstrate the complementary performance of the direct (baseband) and AOM (heterodyne) channels. For instance, at operating point 1 (direct arm at fringe midpoint, slope ≈ 0), the direct channel yields ultrasound amplitudes of ±0.1 V with a stable DC level of ~1 V, while the AOM channel exhibits negligible response (~0 V). Conversely, at point 2 (direct arm at reflectance peak, slope = 0), the AOM channel achieves peak sensitivity with ±2 V ultrasound amplitudes and an elevated DC of ~1.6 V, but the direct channel shows no modulation (~0 V). Intermediate points further highlight balanced detection: at point 3 (negative moderate slopes), both channels are active with AOM amplitudes of ±1.5 V and direct amplitudes of ±0.05 V, yielding a lower DC of ~0.4 V; symmetrically, point 4 (positive moderate slopes) produces similar channel responses (±1.5 V for AOM, ±0.05 V for direct) but a higher DC of ~1.4 V. These metrics underscore the system's ability to maintain at least one channel near optimal sensitivity, ensuring reliable ultrasound detection with signal-to-noise ratios suitable for applications such as photoacoustic imaging or nondestructive evaluation.

From a cost-effectiveness perspective, the AOM channel's ultrasound demodulation utilizes a 9.5–11.5 MHz bandpass filter (BPF2) followed by ED, which provides a simple, low-cost solution for extracting the modulated envelope. However, ED inherently requires a minimum input threshold for effective operation; for weak signals (e.g., below ~0.01 V peak), this may lead to incomplete demodulation or increased noise susceptibility. As an alternative, splitting the 10.5 MHz AOM drive signal and mixing it with the BPF2 output via a frequency mixer could enable coherent down-conversion and amplification of faint signals (or, a voltage boosting circuit can be added before the ED), potentially improving sensitivity by 10–20 dB, albeit at the expense of added hardware complexity and cost (e.g., due to the mixer and associated RF components).

While this work presents a high-performance, cost-effective sensor and demodulation scheme validated in a laboratory setting, further optimizations are essential for practical deployment and scalability. For instance, integrating the demodulation electronics onto a compact printed circuit board (PCB) would reduce footprint, enhance portability, and facilitate real-world integration into systems like wearable health monitors or industrial sensors. Additionally, the rear CFPG has been adapted to incorporate a gold-coated disk reflector for improved reflectivity and durability; future enhancements could focus on the frontend CFPG by employing femtosecond laser micromachining techniques to precisely etch the cavity, thereby minimizing fabrication tolerances, reducing material costs, and improving yield without compromising finesse or sensitivity. To comprehensively benchmark the proposed system's performance and demonstrate its competitive advantages in practical applications, further SNR comparisons with existing ultrasound detection devices are necessary.

In summary, the proposed quadrature-biased heterodyne Fabry–Pérot ultrasound sensor offers inherent stability and versatility. By employing a slope-symmetric, angle-tunable gold-disk FP sensor, the design not only extends the usable frequency range of the Fabry–Pérot cavity but also significantly reduces cost. Furthermore, the introduction of dual-channel AOM modulation further lowers the overall system cost while broadening its operational range and applicability. Future research directions include conducting field trials in noisy industrial environments, integrating machine learning algorithms for adaptive wavelength tuning, and exploring multiplexed sensor arrays for distributed sensing applications. These advancements position the technology as a promising and cost-effective alternative for high-fidelity ultrasound detection in biomedical and structural health monitoring domains.

Author Contributions: Conceptualization, Y.C. and M.H.; methodology, Y.C. and M.H.; software, Y.C.; data curation, Y.C. and Z.L.; writing—original draft preparation, Y.C., X.W. and M.A.; writing—review and editing, M.H.; visualization, Y.C. and X.W.; supervision, M.H.; project administration, M.H.; funding acquisition, M.H. All authors have read and agreed to the published version of the manuscript.

Funding: This research was funded by the Office of Naval Research (N000142112273, N000142212321).

Institutional Review Board Statement: Not applicable.

Informed Consent Statement: Not applicable.

Data Availability Statement: The data underlying the results presented in this paper are not publicly available at this time but may be obtained from the authors upon reasonable request.

Acknowledgments: Y. Chu would like to thank Hasanur Rahman Chowdhury for his help with the sensor fabrication and Qiwen Sheng for the technical discussion on FP and AOM modeling.

Conflicts of Interest: The authors declare no conflicts of interest.

References

1. Chu, Y. Research on Technology and Method of Detecting Boundary Layer Parameters Based on Various Lidars. Ph.D. Thesis, University of Science and Technology of China, Hefei, China, 2020.
2. Chanin, M.L.; Garnier, A.; Hauchecorne, A.; Porteneuve, J. A Doppler lidar for measuring winds in the middle atmosphere. *Geophys. Res. Lett.* **1989**, *16*, 1273–1276. [CrossRef]
3. Chu, Y.F.; Liu, D.; Wang, Z.Z. Basic principle and technical progress of Doppler wind lidar. *Chin. J. Quantum Electron.* **2020**, *37*, 580.
4. Karim, F.; Zhu, Y.; Han, M. Modified phase-generated carrier demodulation of fiber-optic interferometric ultrasound sensors. *Opt. Express* **2021**, *29*, 25011–25021. [CrossRef] [PubMed]

5. Wang, Y.; Chu, Y.; Liu, D.; Wu, D.; Wang, Z.; Xing, K.; Kaung, Z.; Wang, B.; Zhong, Z.; Fan, A.; et al. Device for Measuring Transmittance Curve of Fabry-Perot Using Frequency Comb Light Source and Method Using the Same. Patent US11874169B2, 16 January 2024.
6. Omar, A.F. Fiber optic sensors: An introduction for engineers and scientists. *Sens. Rev.* **2013**, *33*. [CrossRef]
7. Lee, B.H.; Kim, Y.H.; Park, K.S.; Eom, J.B.; Kim, M.J.; Rho, B.S.; Choi, H.Y. Interferometric fiber optic sensors. *Sensors* **2012**, *12*, 2467–2486. [CrossRef] [PubMed]
8. Ashry, I.; Mao, Y.; Wang, B.; Hveding, F.; Bukhamsin, A.Y.; Ng, T.K.; Ooi, B.S. A review of distributed fiber–optic sensing in the oil and gas industry. *J. Light. Technol.* **2022**, *40*, 1407–1431. [CrossRef]
9. Wild, G.; Hinckley, S. Acousto-ultrasonic optical fiber sensors: Overview and state-of-the-art. *IEEE Sens. J.* **2008**, *8*, 1184–1193. [CrossRef]
10. Zeng, Y.; Zhang, P.; Li, Z.; Shen, J.; Li, C. Fabry-perot interferometers with resin scaffolders for high sensitivity temperature sensing. *Front. Phys.* **2024**, *12*, 1366488. [CrossRef]
11. Liu, G.; Zhu, Y.; Sheng, Q.; Han, M. Polarization-insensitive, omnidirectional fiber-optic ultrasonic sensor with quadrature demodulation. *Opt. Lett.* **2020**, *45*, 4164–4167. [CrossRef] [PubMed]
12. Chu, Y.; Alshammari, M.; Wang, X.; Han, M. Angle-tunable method for optimizing rear reflectance in Fabry–Perot interferometers and its application in fiber-optic ultrasound sensing. *Photonics* **2024**, *11*, 1100. [CrossRef]
13. Cao, X.; Yang, H.; Li, J.-T.; Li, B.B. Ultrasound sensing with optical microcavities. *Light. Sci. Appl.* **2024**, *13*, 159. [CrossRef] [PubMed]
14. Lv, R.Q.; Guo, P.; Tong, S.; Li, S.Q.; Deng, W. Fiber optic Fabry–Perot ultrasonic sensor for solid-state ultrasonic detection. *IEEE Sens. J.* **2024**, *24*, 20638–20644. [CrossRef]
15. Posada-Roman, J.; Garcia-Souto, J.A.; Rubio-Serrano, J. Fiber optic sensor for acoustic detection of partial discharges in oil-paper insulated electrical systems. *Sensors* **2012**, *12*, 4793–4802. [CrossRef] [PubMed]
16. Chen, Y.; Lu, D.; Xing, H.; Ding, H.; Luo, J.; Liu, H.; Kong, X.; Xu, F. Recent progress in MEMS fiber-optic Fabry–Perot pressure sensors. *Sensors* **2024**, *24*, 1079. [CrossRef] [PubMed]
17. Alshammari, M.; Chu, Y.; Han, M. Real-time in-situ phase sensitivity calibration of interferometric fiber-optic ultrasonic sensors. *Opt. Lett.* **2024**, *49*, 5336–5339. [CrossRef] [PubMed]
18. Dandridge, A.; Tveten, A.B.; Giallorenzi, T.G. Homodyne demodulation scheme for fiber optic sensors using phase generated carrier. *IEEE J. Quantum Electron.* **1982**, *18*, 1647–1653. [CrossRef]
19. Jiang, Y. High-resolution interrogation technique for fiber optic extrinsic Fabry–Perot interferometric sensors by the peak-to-peak method. *Appl. Opt.* **2008**, *47*, 925–932. [CrossRef] [PubMed]
20. Liu, G.; Zhu, Y.; Liu, Z.; Han, M. Passive quadrature demodulation of an ultrasonic fiber-optic interferometric sensor using a laser and an acousto-optic modulator. *Opt. Lett.* **2019**, *44*, 2756–2759. [CrossRef]
21. Chowdhury, H.R. Fiber Optic Fabry-Pérot Interferometric Sensor for Temperature and Strain Measurement. Ph.D. Thesis, Michigan State University, East Lansing, MI, USA, 2023.
22. Chu, Y.; Karim, F.; Wang, X.; Mitul, A.F.; Alshammari, M.; Han, M. Multi-channel Optical Fiber-Coil Ultrasonic Sensor System. In Proceedings of the 31st ASNT Research Symposum, Columbus, OH, USA, 26–30 June 2023.